Journal of Magnetic Resonance 255 (2015) 88–99

Contents lists available at ScienceDirect

Journal of Magnetic Resonance

journal homepage: www.elsevier.com/locate/jmr

Efficient 2D MRI relaxometry using compressed sensing

Ruiliang Bai [a,b], Alexander Cloninger [c], Wojciech Czaja [d], Peter J. Basser [a,*]

[a] Section on Tissue Biophysics and Biomimetics, PPITS, NICHD, National Institutes of Health, Bethesda, MD 20892, USA
[b] Biophysics Program, Institute for Physical Science and Technology, University of Maryland, College Park, MD 20740 USA
[c] Applied Mathematics Program, Yale University, New Haven, CT 06511, USA
[d] Department of Mathematics, Norbert Wiener Center, University of Maryland, College Park, MD 20742, USA

ARTICLE INFO

Article history:
Received 19 January 2015
Revised 3 April 2015
Available online 11 April 2015

Keywords:
Relaxation
2D relaxometry
Compressed sensing
MRI
Inverse Laplace transform
Exchange
Rician noise

ABSTRACT

Potential applications of 2D relaxation spectrum NMR and MRI to characterize complex water dynamics (e.g., compartmental exchange) in biology and other disciplines have increased in recent years. However, the large amount of data and long MR acquisition times required for conventional 2D MR relaxometry limits its applicability for *in vivo* preclinical and clinical MRI. We present a new MR pipeline for 2D relaxometry that incorporates compressed sensing (CS) as a means to vastly reduce the amount of 2D relaxation data needed for material and tissue characterization without compromising data quality. Unlike the conventional CS reconstruction in the Fourier space (k-space), the proposed CS algorithm is directly applied onto the Laplace space (the joint 2D relaxation data) without compressing k-space to reduce the amount of data required for 2D relaxation spectra. This framework is validated using synthetic data, with NMR data acquired in a well-characterized urea/water phantom, and on fixed porcine spinal cord tissue. The quality of the CS-reconstructed spectra was comparable to that of the conventional 2D relaxation spectra, as assessed using global correlation, local contrast between peaks, peak amplitude and relaxation parameters, etc. This result brings this important type of contrast closer to being realized in preclinical, clinical, and other applications.

© 2015 Published by Elsevier Inc.

1. Introduction

The power of NMR spectroscopy was significantly increased by the inclusion of a second dimension in the Fourier domain, expanding the ability to determine molecular structure, dynamics, and kinetics [1]. In recent years, there have also been increasing numbers of important developments and novel applications of multi-dimensional MR relaxometry to characterize the microstructure-related water dynamics (multiple components, exchange, correlations, etc.) in biological tissue [2–10], food sciences [11,12], material sciences [13–16], porous media physics [17–19], and geophysics [20,21].

NMR relaxometry has been further advanced by the development of novel multi-dimensional diffusion/relaxation pulse sequences [8,13,19,22–26] and robust and accurate two-dimensional (2D) inverse Laplace transform (ILT) algorithms and data analysis methods [27–31]. However, the large amount of MR relaxation data and long scan times required for 2D relaxometry render this method infeasible and impractical for most preclinical and clinical applications. Faster data acquisition, improved experimental designs, and more efficient data reconstruction methods requiring a reduced amount of data are highly desired to make 2D relaxometry practicable.

Recently, compressed sensing (CS) was introduced and successfully applied in the MRI field to accelerate data acquisition [32–37]. The conventional CS is mainly performed on the reconstruction in the Fourier space (k-space), which relies on the sparsity of the MRI images. However, to our best knowledge, no attention has been paid to the possibility of direct CS reconstruction from undersampled 2D relaxation signals, denoted as Laplace space.

One widely used 2D ILT algorithm used in 2D relaxometry was developed by Venkataramanan, et al. about a decade ago [27,28]. In their algorithm, it was shown that the 2D relaxometry signal could be compressed into a small matrix without losing useful information, which demonstrates the sparsity of the 2D relaxometry signal in some basis representations [32,38,39]. Noticing that, a natural question it raises is whether CS could be adopted to reduce the amount of data required for 2D relaxometry. Unfortunately, the authors in [27,28] only focused on compressing data to reduce the computation memory required to and accelerate the calculation of 2D relaxation spectra.

Recently, inspired by these findings, we proved the feasibility of the CS for the 2D relaxometry in theory and developed an efficient

* Corresponding author. Fax: +1 301 435 5035.
E-mail address: pjbasser@helix.nih.gov (P.J. Basser).

http://dx.doi.org/10.1016/j.jmr.2015.04.002
1090-7807/© 2015 Published by Elsevier Inc.

CS algorithm to reconstruct the 2D relaxometry from undersampled 2D relaxometry signals directly [39]. Using numerical simulations, the efficiency of the CS algorithm was used to recover 2D relaxometry using a vastly reduced number of MR measurements [39].

In this work, we develop and systematically demonstrate an MR experimental data analysis pipeline to apply this newly proposed CS algorithm to real experimental 2D relaxation spectra with a vastly reduced data set, suitable for material and tissue characterization without compromising data quality. This is an important development and test of the algorithm to find out the potential systematic artifacts in experiments and the best acceleration factor that can be achieved for each 2D relaxation spectra from various samples.

We illustrate this new approach using MR data obtained on a 7 T vertical wide-bore Bruker MRI scanner similar to those used in preclinical imaging applications. Both T_1–T_2 and T_2–T_2 relaxometry NMR data were acquired on a well-characterized urea/water phantom, which shows two exchanging components. T_1–T_2 MRI relaxometry was also performed on a fixed porcine spinal cord. In addition, numerical simulations of the 2D relaxation spectra were used to assess the effects of noise on the CS-based reconstruction of the 2D ILT.

2. Materials and methods

2.1. Experiments

2.1.1. Urea/water phantom

The aqueous urea model system has been chosen for this study since it has two distinguishable types of protons in the transverse relaxation time (urea proton has a shorter T_2 than water proton) and urea is highly soluble in water [23,40]. A 7 M-urea solution was made by dissolving urea powder (Sigma–Aldrich, Inc., USA) into phosphate buffered saline (PBS, pH = 7.4), resulting in a urea/water proton ratio of 20%/80%. Then, 0.2 mM Gd-DTPA (Magnevist®; Berlex, Inc.) and 0.025 μM $MnCl_2$ were added to the urea solution to reduce relaxation times. The pH of the urea solution was titrated to 8.1 with NaOH. An 80 μL solution was then transferred to a 5 mm susceptibility-matched Shigemi NMR tube (Shigemi Inc., Japan). All NMR experiments were completed within 24 h after the solution was prepared to ensure stability of the phantom [23,40].

2.1.2. Porcine spinal cord

Porcine spinal cord was excised after necropsy and immediately immersion fixed in a 4% formalin solution. All animal handling protocols were approved by the NIH Heart, Lung, and Blood Institute (NHLBI) Animal Care and Use Committee. Prior to the MRI experiments, the spinal cord was washed and fully rehydrated with PBS and then placed in a 10 mm susceptibility-matched Shigemi NMR tube (Shigemi Inc., Japan) with Fluorinert (3 M, St. Paul, MN) filling the open spaces during the MRI experiments.

2.1.3. NMR and MRI measurements

Both the NMR measurements of the urea/water phantom and the MRI experiments on the fixed spinal cord were performed on a 7 T Bruker vertical-bore microimaging μMRI scanner equipped with an Avance III console, and a micro2.5 microimaging gradient system (Bruker BioSpin, Billerica, MA). All specimens were kept at a bore temperature (≈17 °C) during scanning.

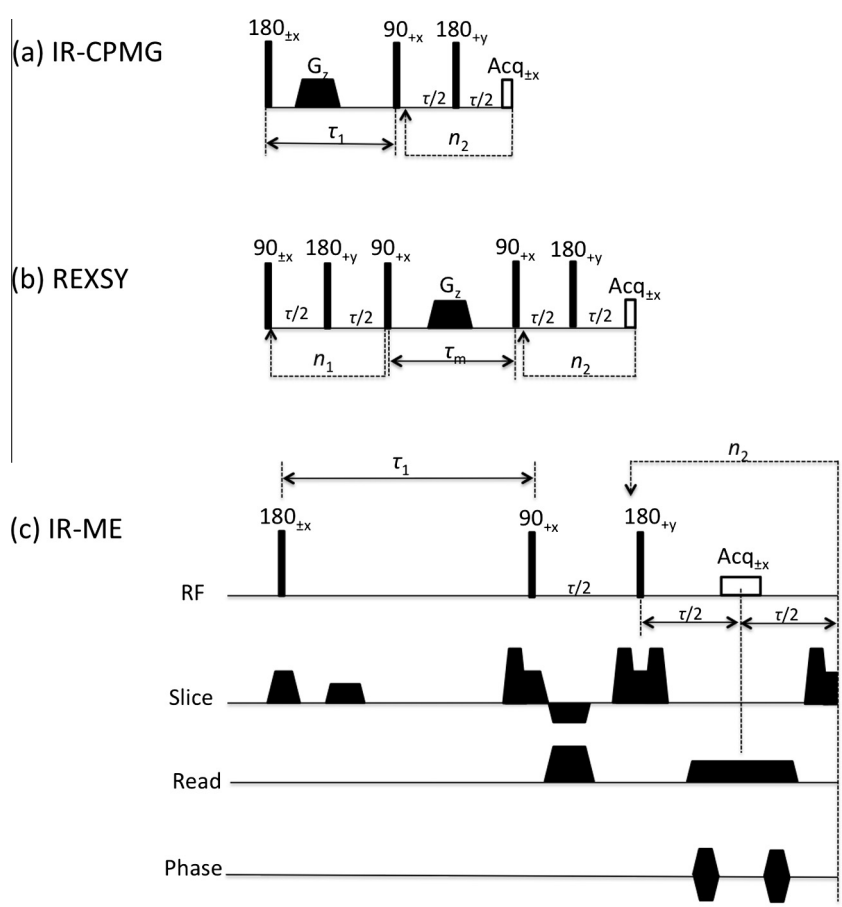

Fig. 1. Pulse sequences diagrams for the three pulse sequences used in this work: (a) IR-CPMG, (b) REXSY, and (c) IR-ME with imaging. τ_1 is the inversion delay, τ is the echo time in the CPMG, τ_m is the mixing time in the REXSY, n_1 and n_2 are the number of loops in the first and second dimensions.

2.1.4. 2D NMR of urea/water phantom

Two different 2D NMR relaxometry pulse sequences were performed on the urea/water phantom: (a) T_1–T_2 correlation relaxometry was performed using an inversion–recovery (IR) preparation "filter," followed by Carr–Purcell–Meiboom–Gill (CPMG) pulse trains (IR-CPMG) (Fig. 1a); (b) T_2–T_2 exchange relaxometry was performed using relaxation exchange spectroscopy (REXSY) (Fig. 1b), which consists of two CPMG pulse trains separated by a mixing time, τ_m, during which the magnetization is stored back along the longitudinal axis. A gradient spoiler was placed after the IR pulse in the IR-CPMG sequence and during the mixing period in the REXSY sequence to "crush" any remaining magnetization in the transverse plane.

In the IR-CPMG pulse sequence, 50 IR points were sampled logarithmically from 50 ms to 5 s; 250 echoes were acquired in the CPMG pulse trains with a temporal spacing of $\tau = 2$ ms. The prescan delay was set to 15 s to ensure full inversion recovery. A two-step phase cycling scheme was used (Fig. 1a), and only one repetition was acquired. An equilibrium CPMG echo train was also acquired with an inversion–delay of 15 s and four repetitions. In the REXSY experiments, the same parameters were used as in the IR-CPMG experiments, with the mixing time, τ_m, starting from 50 ms, and then 100 ms and then in 100 ms steps until reaching 1000 ms. The repetition time (TR) was 8 s.

2.1.5. T_1–T_2 MRI of porcine spinal cord

T_1–T_2 correlation relaxometry was performed by an IR-prepared multiple spin echo (ME) sequence (Fig. 1c) with 36 inversion delays logarithmically distributed from 260 ms to 5000 ms and 50 spin echoes starting at 5 ms and continuing to 250 ms in 5 ms increments. The other acquisition parameters were: TR = inversion-delays + 12 s, matrix size = 64 × 64, slice thickness = 1 mm, field of view (FOV) = 10 mm × 10 mm, and a two-step phase cycling. Hermite pulse shapes were applied for both excitation and refocusing pulses with bandwidth (5400 Hz) matching and proper gradient crasher, and a 5 ms hyperbolic secant inversion pulse was used for uniform inversion of the sample. A magnetization equilibrium scan was also acquired with an inversion–delay equal to 12 s with four repetitions.

2.2. Theory and data analysis

The following data analysis flowchart (Fig. 2) was developed and used in this work to validate and test the efficiency of the CS framework. Experiments with dense sampling points were first performed to approximate the ground truth. After the raw data were preprocessed, 2D relaxation spectra were calculated from the full data set via 2D ILT. Random samples were then obtained from the preprocessed full data with different acceleration factors, R (where $1/R$ is the fraction of the full data). The subsamples were then processed using two pipelines: CS reconstruction and conventional 2D ILT reconstruction. 2D relaxation spectra from each subsample were then compared to the result obtained from the full data, in the experiments, or to the ground truth, in the simulations.

2.2.1. Preprocessing

To remove the bias caused by Rician noise in the IR-ME MRI data, the noisy ME MRI magnitude data were first processed by a methodology we proposed and validated previously to transform 1D Rician magnitude data to Gaussian-distributed data [41–43]. Furthermore, region of interest (ROI) analysis was performed to satisfy the signal-to-noise ratio (SNR) requirements of the 2D ILT, which generally needs a high SNR to obtain stable and accurate solutions. Here ROIs in white matter with a relatively homogenous geometric mean T_2 (gmT_2) were selected.

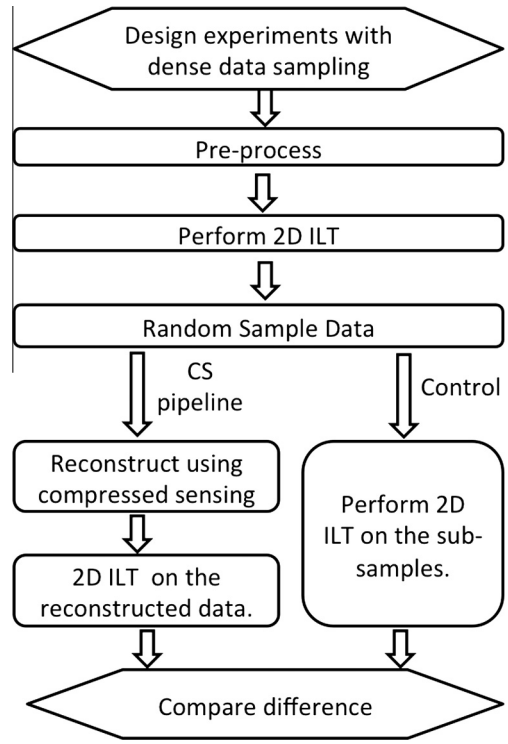

Fig. 2. Flowchart of the pipeline used in this work.

In the IR-CPMG and IR-ME experiments, the CPMG and ME data were subtracted from the corresponding equilibrium data to cancel the potential artifacts caused by imperfect 180° inversion pulses. Then, the experimental data from all three pulse sequences can be written as:

$$M(\tau_1,\tau_2) = \sum_{m=1}^{N_m}\sum_{n=1}^{N_n} F(T_m,T_n)\exp\left(-\frac{\tau_1}{T_m}\right)\exp\left(-\frac{\tau_2}{T_n}\right) + \epsilon(\tau_1,\tau_2) \quad (1)$$

where τ_1 is the inversion delay in the T_1–T_2 sequences and the accumulated echo time $n_1\tau$ of the first CPMG in the T_2–T_2 sequences; τ_2 is the accumulated echo time $n_2\tau$ of the second CPMG or ME; $F(T_m, T_n)$ is the 2D probability density function (pdf) of the two corresponding relaxation parameters; N_m and N_n are the number of sampling points in each dimension of F; and $\varepsilon(\tau_1, \tau_2)$ is the noise, which is assumed to be Gaussian in most 2D ILT algorithms. Here $N_m = 100$ and $N_n = 100$ were set for all of the following analysis.

2.2.2. 2D ILT

Inversion of the 2D LT is generally ill-conditioned; a small change in M may result in large variations in $F(T_m, T_n)$. One practical technique to obtain a stable solution is minimizing Ξ:

$$\Xi \equiv \sum_{i=1}^{N_1}\sum_{j=1}^{N_2}\left[M(\tau_i,\tau_j) - \sum_{m=1}^{N_m}\sum_{n=1}^{N_n} F(T_m,T_n)\exp\left(-\frac{\tau_i}{T_m}\right)\exp\left(-\frac{\tau_j}{T_n}\right)\right]^2 + \alpha\sum_{m=1}^{N_m}\sum_{n=1}^{N_n} F(T_m,T_n)^2 \quad (2)$$

with a data-quality term with nonnegative constraints on F, and a second term for Tikhonov regularization. Above, N_1 and N_2 are the number of measurements in the first and second dimension, and

α is the regularization parameter. Eq. (2) can be rewritten in the form of a kernel matrix for the full data:

$$\Xi \equiv \left\| M - K_1 F K_2'^2 \right\|^2 + \alpha \|F\|^2 \tag{3}$$

where $\|\cdot\|$ is the Frobenius norm of a matrix, and K_1 and K_2 are the kernels of the first and second dimension with the matrix size $N_1 \times N_m$ and $N_2 \times N_n$.

Here, a fast and widely used algorithm proposed by Venkataramanan et al. [28] to solve the minimization problem was applied. In this algorithm, the data are partially compressed by using the singular value decomposition (SVD) of K_i

$$K_i = U_i S_i V_i' \quad i \in \{1, 2\} \tag{4}$$

By truncating the small singular values with a threshold (1×10^{-3} of the largest single value), S_i can be reduced to a much smaller matrix with dimensions $N_i \times s_i$. Then, the data matrix M can be projected onto the column space of K_1 and the row space of K_2 with a much smaller dimension: $\widetilde{M} = U_1' M U_2$ with the new matrix size $s_1 \times s_2$ [27,28]. Now Eq. (3) can be rewritten in an identical structure, but with the compressed data $\widetilde{M}$ and kernels of a much lower dimension [27,28,39].

For a given value of the regularization parameter, α, a unique solution can be obtained from Eq. (2) or Eq. (3) by solving the constrained optimization problem. An S-curve based method, which calculates the fitting error to the measurements $\chi(\alpha)$ with a series of α, was used to robustly determine the optimal value of α [27,31,44]. The best α is chosen within a user-defined tolerance, TOL:

$$d(log_{10}\chi(\alpha))/d(log_{10}\alpha) = \mathrm{TOL} \tag{5}$$

Here TOL = 0.1 was used for both the simulated data and the experimental data.

2.2.3. Subsampling

After preprocessing the raw data, 1000 random subsamples were obtained from the full data at each different acceleration factor, R, by randomly sampling in the 2D relaxometry data matrix. The subsamples were then reconstructed using CS, and 2D relaxation spectra were then calculated from the reconstructed data via 2D ILT with data compression. As a control, conventional 2D ILT without data compression was directly performed on the subsamples as in Eq. (2).

2.2.4. Brief review of the CS algorithm for 2D-ILT reconstruction

The key concept behind CS reconstruction lies in the relationship between the full data matrix M and the compressed data $\widetilde{M}$. Because $M = U_1 \widetilde{M} U_2'$, and because U_1 and U_2 are left orthogonal and have energy spread out across M, these measurements form an incoherent, tight frame [39]. It means each element of M is an observation of a dense linear combination of every element of $\widetilde{M}$ simultaneously. $\widetilde{M}$ also has rapidly decaying singular values. For these reasons, and the fact that $\widetilde{M}$ has much smaller dimensions than M, one can capture all the information in $\widetilde{M}$ with a fraction of the number of measurements in M.

The reconstruction algorithm to recover $\widetilde{M}$ is also based on the fact that $\widetilde{M}$ has rapidly decaying singular values. The algorithm is a modification of the singular value thresholding algorithm from Cai et al. [45]. This optimization problem searches for the matrix X that minimizes the sum of the singular values, while matching the measurements $M = U_1 X U_2'$. The solution to this optimization problem, then, has a high probability, close to $\widetilde{M}$, of being up to a constant factor of the noise [39]. Some brief steps of the proposed CS reconstruction were summarized in Appendix A and more information can be found in [39].

2.2.5. Comparison

Global similarities were obtained for the pdf, F, from the full data or the ground truth and one from each subsample by calculating a correlation coefficient (C) between all of the vectorized versions. In addition, the geometric mean (gm) relaxation parameters and the relative volume fraction (f) of each peak in each 2D relaxation spectra were also calculated and compared to the results from the full data or ground truth. The results of each 1000 realizations were displayed as Tukey box plots, in which the notch is the median, the edges of the box are the 25th and 75th percentiles, the whisker length is 1.5, and the outliers are plotted separately. Further, the paired Student's t-test was performed on the correlation coefficients from the results of the CS reconstruction and the control with the null hypothesis that C are equal in the results via the two methods and the alternative hypothesis that C is higher in the CS reconstruction than the control. Fisher z-transformation was applied on the correlation coefficients before the hypothesis test.

The median of the 1000 2D relaxation spectra data from all subsamples at each R is displayed and the variance of the results is characterized by interquartile range (IQR). The contrast between the two peaks is defined by the ratio of the smallest amplitude between the two components over the smaller component's amplitude in the T_2 projection of the displayed 2D relaxometry.

2.3. Simulations

T_1–T_2 relaxometry experiments were simulated by a Monte Carlo method to further test and validate the efficiency of the proposed CS reconstruction. The data acquisition protocol used in the T_1–T_2 MRI of spinal cord was applied here. Two broad peaks without exchange in the 2D T_1–T_2 relaxogram with positions and patterns similar to those obtained from spinal cord white matter were used as the joint pdf, F, to generate the data following Eq. (1) with Gaussian noise at various SNRs. Stable estimates were obtained by performing 1000 realizations for the full data with one random sample taken for each acceleration factor in each realization.

Furthermore, the potential artifacts caused by Rician noise were also simulated. An ROI consisting of 100 voxels with an IR-ME sequence was synthesized. Within each voxel, the data M_R were generated by changing the distribution of the signal in Eq. (1) from Gaussian to Rician at SNR = 200:

$$M_R(\tau_1, \tau_2) = \sqrt{\left[\sum_{m=1}^{N_m}\sum_{n=1}^{N_n} F(T_m, T_n)\exp\left(-\frac{\tau_1}{T_m}\right)\exp\left(-\frac{\tau_2}{T_n}\right) + \epsilon_1(\tau_1, \tau_2)\right]^2 + \epsilon_2(\tau_1, \tau_2)^2} \tag{6}$$

where ϵ_1 and ϵ_2 are Gaussian noise. The averaged data in the ROI were taken as the complete data set (SNR = 2000) with 1000 repetitions. The following subsampling and data analysis was the same as described in Section 2.2 and the simulations with Gaussian noise.

3. Results

3.1. Simulations

3.1.1. Noise type

For the full data with Gaussian noise at SNR = 2000, the 2D ILT algorithm yields a close estimate (Fig. 3b) of the ground truth (Fig. 3a) with a correlation coefficient $C = 0.92$ (Fig. 3g). Uncorrected Rician noise introduces spurious peaks in the long-

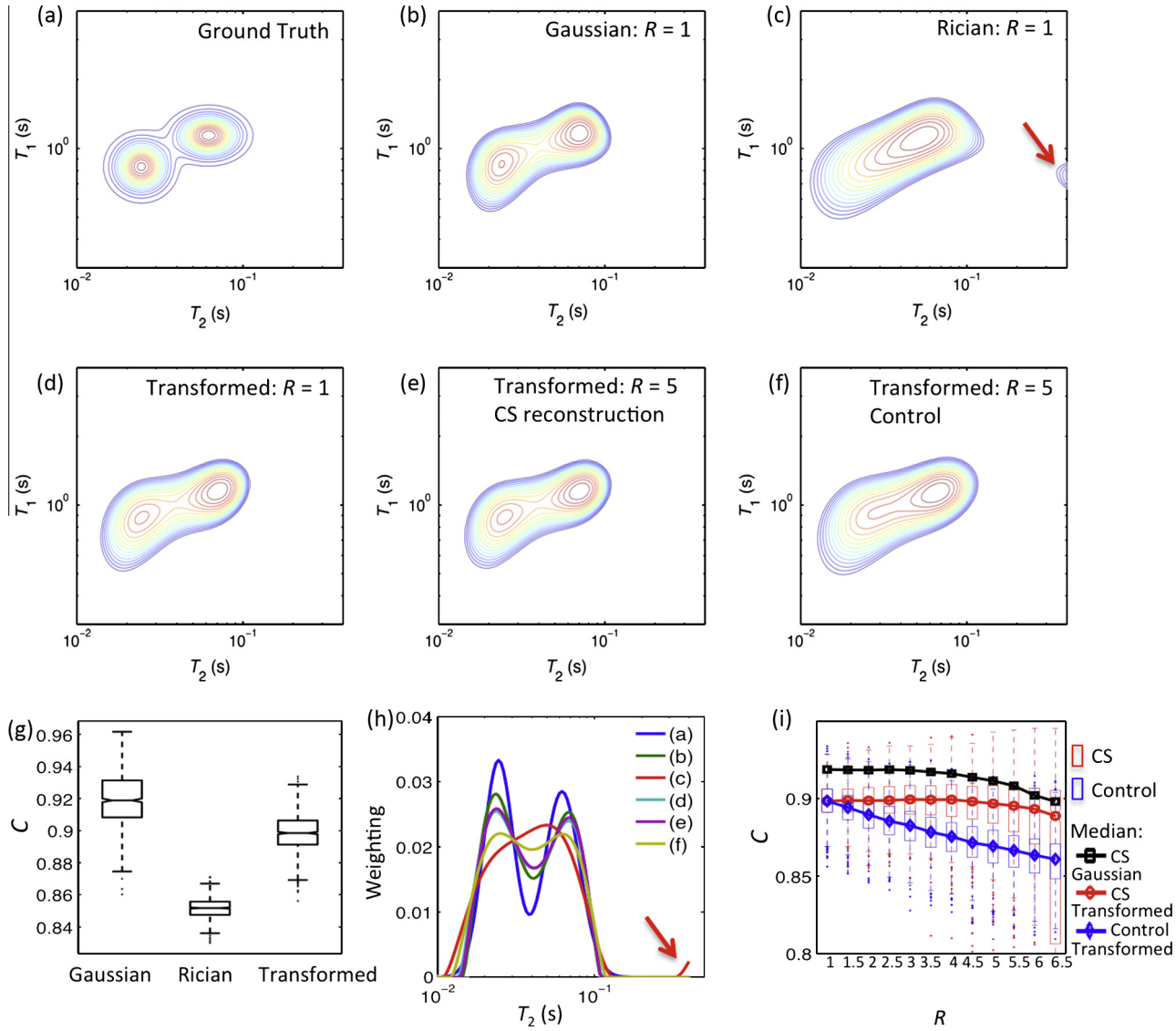

Fig. 3. 2D T_1–T_2 relaxometry of (a) the simulated ground truth, (b) full data with Gaussian noise at SNR = 2000, (c) full data with magnitude signal, (d) full data with transformed (Rician noise corrected) signal, (e) CS reconstruction from the transformed data at $R = 5$ and (f) the corresponding control. (g) The results of the correlation coefficients of (b–d). (h) The normalized T_2 projections of (a–f). (i) The results of the correlation coefficients of the CS reconstruction from the data with Gaussian noise (black), the transformed signals from magnitude data (red) and its corresponding control (blue) at various acceleration factors, R. (For interpretation of the references to color in this figure legend, the reader is referred to the web version of this article.)

T_2 regime, which are visible in both the T_1–T_2 relaxometry (red arrow in Fig. 3c) and its 1D projection onto the T_2 axis (red arrow in Fig. 3h). In addition, the two peaks are merged indistinguishably into one in both the T_1 and T_2 dimensions. The application of the signal transformation correction successfully removes the spurious peaks and makes the ground-truth peaks distinguishable (Fig. 3d and h) concomitant with the recovery of the correlation coefficient from 0.85 to 0.90 (Fig. 3g).

Subsampling was performed both on the data with Gaussian noise and on the data with the transformed signal. The results are shown in Fig. 3i, in which only the median was plotted for the data with Gaussian noise for display. Within the transformed data, the CS reconstruction successfully achieves a high correlation coefficient $C \sim 0.90$ with a small variance until R reaches 5, which is significantly higher than the results of the control ($p < 1 \times 10^{-9}$). Except for the higher correlation coefficients, better contrast is also observed with CS reconstruction. For example, at $R = 5$, the contrast between the two peaks is 69% with the CS reconstruction, but 89% in the control, where the ground truth is 34%.

3.1.2. Noise amplitude

The quality of the T_1–T_2 spectra from the full data itself decreases as the SNR in the simulations with Gaussian noise decreases (Fig. 4). For example, the correlation coefficients drop from 0.94 to 0.84 when the SNR decreases from 10,000 to 200 (Fig. 4l). Except for the decrease in the correlation coefficient, the contrast between the two peaks is also artificially reduced owing to the larger noise amplitude, which can be seen by comparing the T_1–T_2 spectrum with different noise amplitudes (Fig. 4a–c). The contrast in the 1D T_2 projection is changed from 60% to 85% when the SNR drops from 2000 to 800, where the two peaks are indistinguishable at SNR = 200.

The CS reconstruction from subsamples successfully maintains the quality of T_1–T_2 spectra at similar levels as the results form the full data when the SNR decreases. At $R = 3$, the correlation coefficients from the subsample with CS reconstruction shows almost identical distributions as the results from the full data with slightly larger variance ($\leqslant$1.5 times higher IQR) until the SNR drops below 800. At $R = 5$, the correlation coefficients drops a little with larger

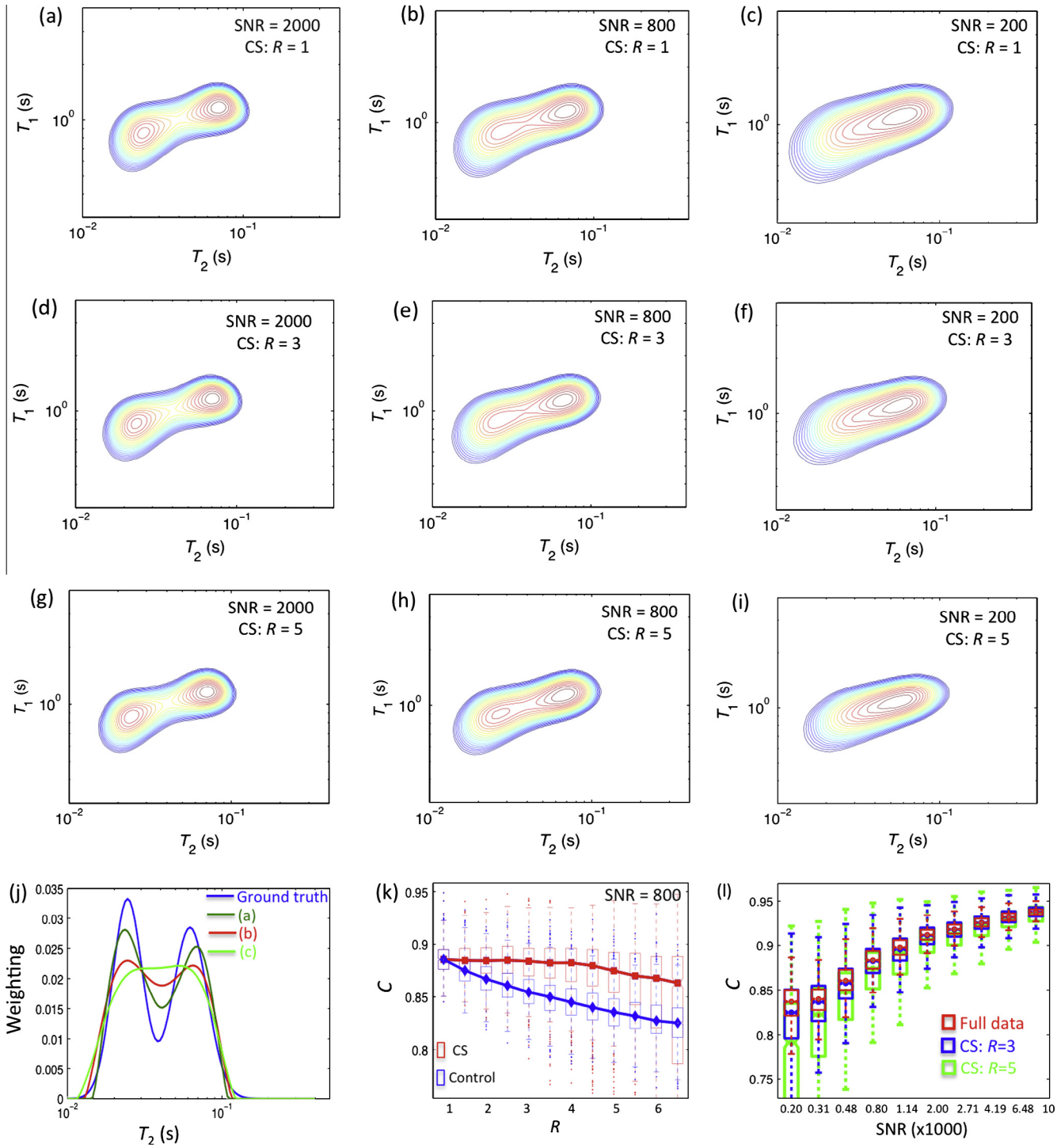

Fig. 4. (a–i) T_1–T_2 relaxometry from the stimulated data with Gaussian noise at three SNR levels (SNR = 2000, 800, and 200) and three acceleration factors: $R = 1$, 3, and 5. (j) The normalized T_2 projections of (a–c) and the ground truth. (k) The boxplots of the correlation coefficients of the CS reconstruction (red) and the control (blue) from the simulated data with Gaussian noise at SNR = 800 at various acceleration factors, R, and the broader lines and dots are the median of the data at each R. (l) The boxplots of the correlation coefficients of the full data (red), CS reconstruction at $R = 3$ (blue), and $R = 5$ (green) at various SNR. For the display, the outliers were not shown. (For interpretation of the references to color in this figure legend, the reader is referred to the web version of this article.)

variance, especially at lower SNR (<2000). Compared to the control, the results from CS reconstruction show much better quality at certain acceleration factors. For example, at SNR = 800, the correlation coefficients from the CS reconstruction results are significantly higher than the control ($p < 5 \times 10^{-9}$) until $R \geqslant 5.5$ (Fig. 4k). At higher R, the sample size is not large enough to generate good-quality T_1–T_2 spectra via either the CS reconstruction or the conventional 2D ILT.

3.2. Urea/water T_1–T_2 spectra

Here, only the fourth echoes of the 250 CPMG echo trains were used; as a result the matrix size of the full data acquisition is 50×62 with SNR $\geqslant 5000$. The T_1–T_2 spectrum from the full data is shown in Fig. 5a, in which two peaks are clearly observed: urea with gmT_2 = 30.9 ms, gmT_1 = 618 ms, and f = 18.9%; and the water with gmT_2 = 156 ms, gmT_1 = 614 ms, and f = 81.1%. The small bias

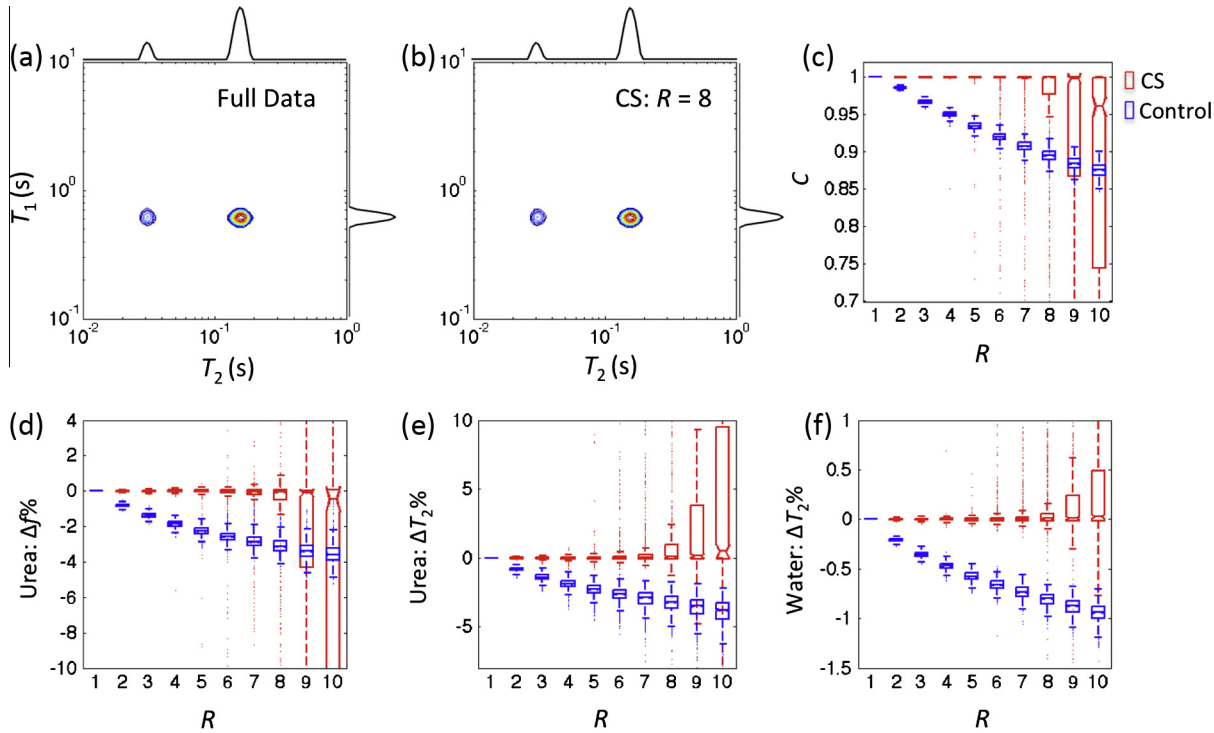

Fig. 5. T_1–T_2 spectra of the urea/water phantom from (a) the full data and (b) the CS reconstruction at $R = 8$, in which the curves along the axes are the 1D projections onto each dimension. (c–f) are the Tukey box plots of the results from the 1000 realizations in each acceleration factor R, which includes (c) the correlation coefficients, the percentage of the biases of the urea's (d) relative volume fraction and (e) gmT_2 and (f) the water's gmT_2.

of the relative volume fractions from 20%/80% is the result of exchange between the protons on the urea molecules and those on the water molecules. The projections of the T_1–T_2 distribution onto the T_1 and T_2 axes are shown along the axes in Fig. 5a and b. A single peak is observed in the projected 1D T_1 spectrum with gmT_1 = 614 ms for both the full data and CS reconstruction at $R = 8$. Two peaks are observed in the projected 1D T_2 spectra for which the full data set is used with $f = 18.9\%$ and gmT_2 = 30.9 ms for the urea and $f = 81.1\%$ and gmT_2 = 156 ms for the water. The corresponding values at $R = 8$ with CS reconstruction are $f = 18.6\%$ and gmT_2 = 30.9 ms for the urea and $f = 81.4\%$ and gmT_2 = 156 ms for the water.

In Fig. 5b, the T_1–T_2 spectrum at acceleration factor $R = 8$ is presented; this spectrum has a very high correlation coefficient, $C > 0.999$. In contrast, the corresponding value of 1000 simulations in the control at $R = 8$ drops to 0.895 as shown in Fig. 5c, which is significantly smaller than the CS reconstruction ($p < 1 \times 10^{-9}$). With CS reconstruction at $R \leqslant 8$, the biases of the urea parameters are: $\leqslant$0.1% for the f, $\leqslant$0.1% for the gmT_1, and $\leqslant$1% for the gmT_2. The corresponding values for the water are: $\leqslant$0.02%, $\leqslant$0.02%, and $\leqslant$0.01%, respectively. In contrast, the corresponding biases in the control at $R = 8$ are −3.1%, −0.2%, and −3.2% for the urea and 0.73%, 0.09%, and 0.80% for the water. In addition, the variance of the results obtained with 1000 random samples is much smaller than that of the control at $R \leqslant 6$ and comparable to the control at $R = 7$ and 8. At a higher acceleration factor ($R \geqslant 9$), very large variance and growing bias are observed.

3.3. Urea/water T_2–T_2 spectra

T_2–T_2 spectra of the urea/water phantom at different mixing times are shown in Figs. 6a and 7a. As the mixing time becomes longer, the total signal intensity decreases while the relative fraction of the off-diagonal peaks increases. A two-site exchange model was used to fit the amplitudes of the peaks following a similar protocol as proposed by Does et al. [23] with the estimate of the urea proton fraction being 19.6% and the exchange rate 0.35 s^{-1}. Two peaks at $\tau_m = 50$ ms and $\tau_m = 1000$ ms, with SNRs of ~5000 and 1000 respectively, were chosen to test the performance of the CS reconstruction.

At $\tau_m = 1000$ ms, the off-diagonal peaks (P_{ab} and P_{ba}) appear with the total relative volume fraction 15.1%, for which the relative volume fractions of the unchanged urea (P_{aa}) and the water (P_{bb}) are 11.3% and 73.6% respectively. At $R \leqslant 9$, the correlation coefficients between the CS reconstructed T_2–T_2 spectra and the one from full data can be maintained as high as $\geqslant$0.989, which are significantly higher than the control ($p < 1 \times 10^{-9}$); this coefficient begins to fall quickly with larger variance at $R \geqslant 10$. In the control, there is a strong underestimation of the relative fraction of the off-diagonal peaks, $P_{ab} + P_{ba}$, and an overestimation of the water peaks P_{bb}, which can be as large as 14.5% and 1.8% at $R = 9$. CS reconstruction successfully corrects the biases back (e.g., 1.1% (overestimation) and 0.36% (overestimation) at $R = 9$), with almost the same variance at low R and a slightly larger variance at high R (e.g., ~1.8 times higher in IQR than the control at $R = 9$). Except for the precise reconstruction of each peak's relative fraction, the other relaxation parameters are also more accurate. For example, the gmT_2 of the peak P_{ab} is underestimated by 8.2% and 3.1% at the first and second dimension (gm$T_{2,1}$ and gm$T_{2,2}$) in the control case at $R = 9$, while the overestimations of peaks in the CS reconstruction are only 1.6% and 0.24%.

At mixing time, $\tau_m = 50$ ms, good CS reconstruction can be obtained until $R = 12$. Here the 125 × 125 data matrix was first evenly subsampled into a 62 × 62 matrix ($R = 4$); then additional subsampling was performed randomly on the 62 × 62 data matrix. In Fig. 7b, the statistical median of the 1000 T_2–T_2 spectra at $R = 12$ is shown; the correlation coefficient, $C = 0.962$, is very close to the corresponding value (0.964) at $R = 4$. At $R \leqslant 12$, the statistical estimations of the other relaxation and amplitude parameters are also accurate and precise: for example, the median biases of the f,

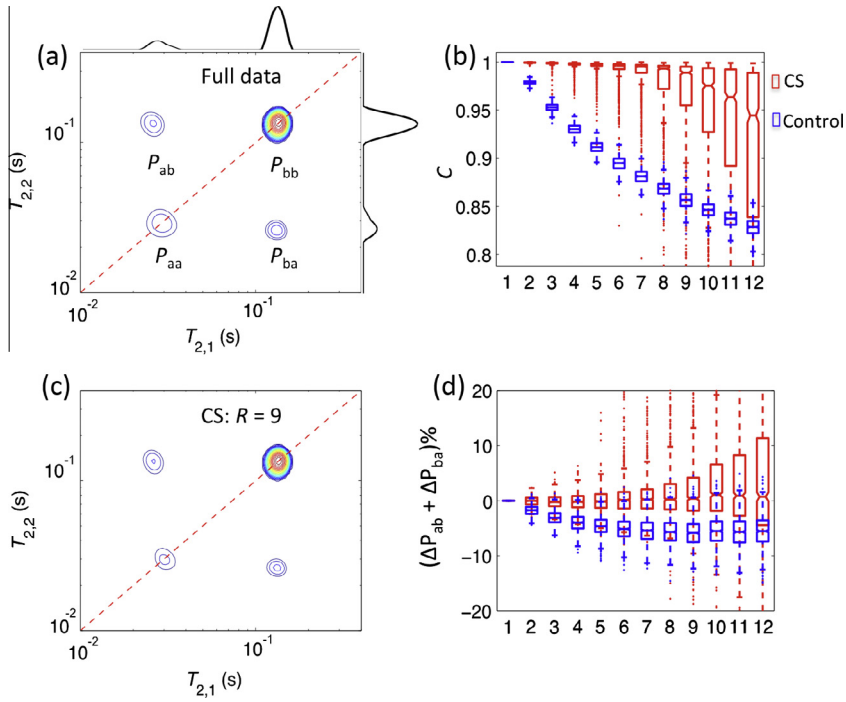

Fig. 6. T_2–T_2 spectra of the urea/water phantom at mixing time $\tau_m = 1000$ ms from (a) the full data and (c) the CS reconstruction at $R = 9$. (b and d) are the results of (b) the correlation coefficients and (d) the biases of the relative volume fractions of the off-diagonal peaks as a function of the acceleration factor R, for which the red is the CS reconstruction and the blue is the corresponding control. (For interpretation of the references to color in this figure legend, the reader is referred to the web version of this article.)

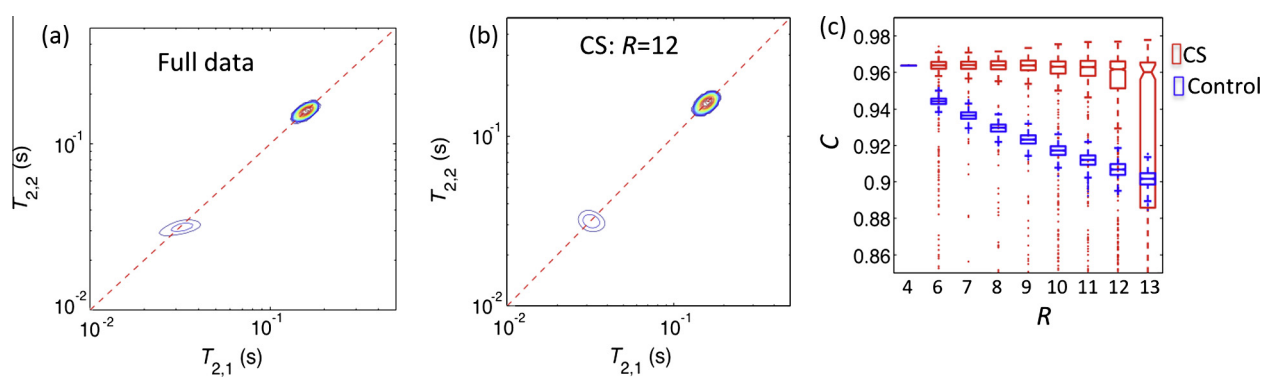

Fig. 7. T_2–T_2 spectra of the urea/water phantom at mixing time $\tau_m = 50$ ms from (a) the full data and (b) the CS reconstruction at $R = 12$. (c) Correlation coefficients as a function of the acceleration factor R, where the red is the CS reconstruction and the blue is the corresponding control. (For interpretation of the references to color in this figure legend, the reader is referred to the web version of this article.)

gm$T_{2,1}$, and gm$T_{2,2}$ of the urea peak are only ⩽0.87%, ⩽0.74%, and ⩽0.45%, respectively, compared with the corresponding results from the full data.

3.4. Porcine spinal cord ROI analysis

The results of the ROI analysis on the dorsal white matter are detailed here (Fig. 8). The SNR in the white matter is approximately 200. Two broad peaks are observed in the T_1–T_2 spectra from the full data (preprocessed) with the myelin water (MW): $f = 46.1\%$, gm$T_2 = 23.8$ ms, and gm$T_1 = 837$ ms, and the intracellular/extracellular water (IEW): $f = 53.9\%$, gm$T_2 = 62.3$ ms, and gm$T_1 = 993$ ms. Here, $T_2 = 35$ ms was used as the separation line between MW and IEW.

As with our simulations, the noisy Rician signals also introduce spurious peaks in the long-T_2 regime (red arrow in Fig. 8d and g), but our signal transformation scheme successfully corrects this artifact. CS performs adequately at $R = 2.5$, for which the correlation coefficient is 0.97 (significantly higher than the control, $p < 1 \times 10^{-4}$) and the contrast between the two peaks is preserved (93% for the CS, 93% for the full data, and a single peak in the control). At $R = 4.0$, the two peaks are still visible although the correlation coefficient (0.91) is lower than the control (0.93) now. Interestingly, the CS reconstruction does well at preserving the MW relative fraction (biases ⩽ 0.41%), though with larger variance, for which the underestimation can be as large as 1.8% in the control at $R = 4.0$. Student's t-test was performed on the results of MW relative fraction from both the CS reconstruction and the control with the null hypothesis that their means are equal to the result from full data. The hypothesis is accepted by the results from CS reconstruction ($p \geqslant 0.15$) except for $R = 4.0$ ($p = 0.02$), while it is rejected by all the results from the control ($p < 1 \times 10^{-7}$).

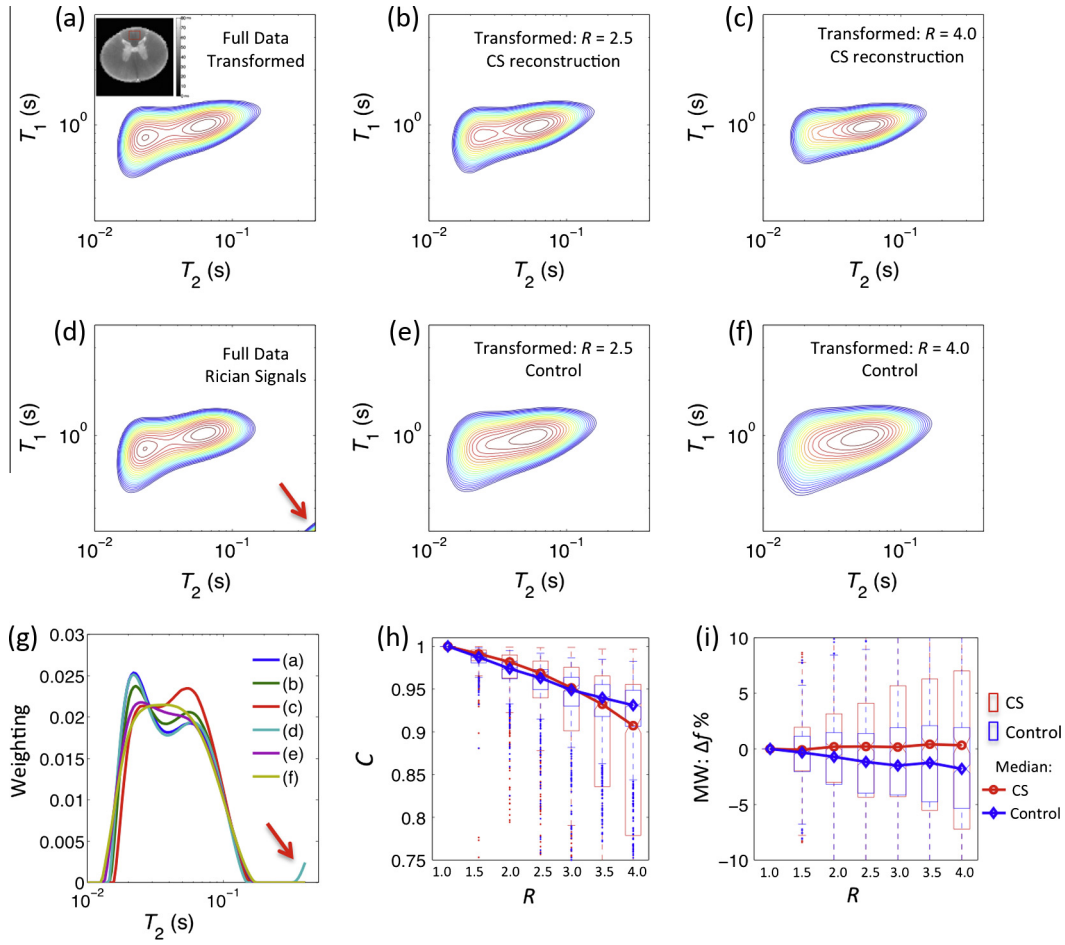

Fig. 8. The T_1–T_2 spectra of (d) the original magnitude data in the dorsal porcine white matter, (a) full data with transformed signal, (b) CS reconstruction from the transformed data at $R = 2.5$ and (c) at $R = 4.0$, (e) and (f) the corresponding control. (g) The normalized 1D T_2 projections of (a–f). (h–g) The results of (h) the correlation coefficients and (i) the MW fraction as a function of the acceleration factor R, where the red are the CS reconstructions and the blue are the corresponding controls. The map of the gmT_2 from 10 ms to 400 ms of the spinal cord and the ROI in the dorsal white matter (red curve) are shown at the upper left corner of (a). (For interpretation of the references to color in this figure legend, the reader is referred to the web version of this article.)

4. Discussion

In this work, our main objective was to design a pipeline to accelerate the acquisition of 2D relaxation spectra using compressed sensing and then to test and validate its efficiency in maintaining the quality of the 2D distributions with both simulations and acquired NMR and MRI experimental data.

Clearly, compared with 1D relaxation spectra, more information can be obtained from the 2D relaxation spectra, even in simple well-defined systems like the urea/water mixture studied here. The 2D spectra can uncover and distinguish different relaxation components that may be hidden in the 1D spectra. For example, only one peak can be observed in the T_1 spectra of the urea/water phantom, whereas two peaks are well defined in the T_1–T_2 relaxation spectra. Furthermore, exchange information between different components can also be extracted from 2D relaxation spectra whereas this is not possible in the 1D case. In T_2–T_2 relaxometry of the urea/water phantom, the off-diagonal peaks provide direct evidence of exchange between the protons on the urea and water molecules; these rates of exchange can be then be quantitatively characterized by modeling and fitting the intensities of the peaks. This information cannot be obtained from 1D T_2 spectra alone.

The 2D-ILT algorithm proposed by Venkataramanan et al. is very sensitive to the SNR and the type of noise. For example, in the simulations, either the change of noise type from Gaussian to Rician or the decreasing of SNR from 10,000 to 200 will significantly affect the quality of the 2D relaxometry. Normally, a high SNR with Gaussian noise is required for good performance. These conditions can be easily achieved for most NMR experiments with large sample sizes at high fields. However, for MRI applications, the SNR is typically lower and the noisy amplitude signal should be transformed from a Rician to a Gaussian distribution. Higher SNR in MRI can be achieved by performing ROI analysis in homogeneous regions.

In both simulations and the MRI experiments on the spinal cord, the presence of Rician noise introduces spurious peaks in the long T_2 regime because the rectification of the complex MR signal produces a "noise floor" which, uncorrected, is fit by the 2D-ILT routine in both dimensions. This baseline signal biases the signal decay, leading to the appearance of artifactually long-T_2 components and decreasing the contrast between existing peaks. This phenomenon is quite similar to the one we observed previously in the 1D T_2 spectra from noisy MRI magnitude data. A signal transformation framework we proposed previously for 1D T_2 spectra in multi-echo MRI is successfully applied here to the 2D relaxation spectra obtained from MRI data to remedy biases caused by Rician noise. While the method is not perfect, these biases are significantly reduced.

CS reconstruction was successfully carried out on the simulated 2D relaxation spectra data, experimental NMR data on a well-

characterized urea/water phantom, and the IR-ME MRI data from the porcine spinal cord. With the CS reconstruction, the size of the data matrix can be reduced significantly without compromising the quality of the final 2D relaxation spectra. Compared with the controls, 2D relaxation spectra obtained from subsamples using CS reconstruction shows a better approximation to the ground truth or to the results from full data, as demonstrated by the higher global correlation coefficient; better contrast between local peaks; and more accurate relative volume fraction and relaxation parameters. A disadvantage of the CS reconstruction is that it admits more outliers at higher R, where the noise in some subsamples causes the CS reconstruction to fail. However, the number of these problematic subsamples becomes negligibly small as a function of the number of data points collected [39]. Additionally, the CS-reconstruction algorithm proposed here is very fast with processing time: approximately several seconds for each reconstruction on an Apple desktop computer with 4 cores.

The maximum acceleration factor, R, that can be achieved using CS reconstruction depends on the noise amplitude, noise type, the experimental design of the MR data acquisition protocol, and the underlying ground truth. In the simulation, better T_1–T_2 spectra are obtained at a high SNR (2000) than at a low SNR (800) at the same acceleration factor. In the T_2–T_2 spectra of the urea/water phantom, $R = 12$ can be achieved at a mixing time, $\tau_m = 50$ ms, but the maximum R at a mixing time $\tau_m = 1000$ ms is 9, for which the SNR is around 5 times lower and the relaxometry spectra appear more complex. As for the simulations of the 2D relaxation spectra with MRI, the maximum R is approximately 5 even after the noise correction, maybe due to that CS is performed with an already small data matrix.

Two distinguishable peaks were observed in the T_1–T_2 spectra of the white matter from the porcine spinal cord, which were assigned to be myelin water (shorter relaxation times) and intracellular/extracellular water (longer relaxation times). These results were consistent with previous 1D T_2 spectra measures in the white matter *in vivo* or *ex vivo* [41,46–48]. Here the maximum R that can be achieved is equal to or less than 4.0, which is smaller than in the simulations. Several reasons may contribute to this reduction: (1) the SNR is lower in the experiments since the number of voxels in the ROI is less than 100; (2) the noise is still not Gaussian even after preprocessing since there might be some systematic artifacts; (3) heterogeneities may exist among voxels and ROI-type analysis might not be the best method; (4) the underlying ground truth of the T_1–T_2 relaxation spectra of the biological tissue is still poorly known, thus there might be biases in the T_1–T_2 relaxation spectra when the complete data set is used. Interestingly, even with a decreased correlation coefficient, CS reconstruction corrects the bias in estimating the MW and IEW fraction with the conventional 2D ILT method, though with larger variance.

The biggest obstacle to migrating 2D relaxation spectra measurement to *in vivo* preclinical and clinical MRI scanning applications is the long acquisition time. For example, the total acquisition time for the IR-ME experiments in this experiment was ~21 h. With CS, the time can be reduced to ~6 h by an acceleration factor $R = 3.5$, but these times are still too long for *in vivo* applications. However, the parameters chosen in our time-consuming IR pulse sequences were conservative, leading to a long pre-scan delay. There are other MRI pulse sequences with shorter acquisition times, such as the saturation-recovery prepared multi-echo (SR-ME) with echo-planer (EPI) acquisition pulse sequences, proposed by Does and Gore [2], whose total acquisition time is about 1 h. If the same acceleration factor $R = 3.5$ can be achieved there, the total acquisition time could be reduced to 17 min. In addition, even higher acceleration factors will be possible as SNR increases with improvements in scanner hardware.

One practical concern of the CS reconstruction is the random sampling, which might be limited by the natural structure of the CPMG or multi-echo pulse trains, i.e., the reduction of the scan time is only achievable in the first dimension of the three pulse sequences (Fig. 1) used in this study. However, in high-field MRI scanners, safety concerns, primarily power deposition in tissue owing to a high specific absorption rate (SAR), limit the total number of 180° pulses that can be applied per unit time. Therefore, a practical alternative would be to use a single echo or a few echoes with a fast MRI acquisition, such as EPI; parallel imaging; and multi-band excitation. In these cases, acceleration provided by CS reconstruction could play an important role in reducing the acquisition time further, making 2D relaxation spectrum MRI measurements clinically feasible. Though the three pulse sequences in this study cannot be directly applied to *in vivo* preclinical and clinical studies, the data from these sequences represents the general 2D relaxometry data structure and the findings in "compressing" the 2D data will be helpful for future pulse sequence designs and data analysis.

In this work, the CS reconstruction was carefully validated in simulations and a limited number of biological samples. For *in vivo* MRI applications, much work is still required, such as reaching a deeper understanding of the ground truth of the 2D relaxation spectra in different biological tissues, better modeling and correction of the noise within MRI acquisitions, and hardware improvements that will increase the SNR. Only 2D T_1–T_2 and T_2–T_2 MR relaxometry were validated here, but this pipeline can be easily adapted to other 2D spectra, such as D–T_2, D–D, and T_1–T_1, provided that the application of the successive "filters" results in a relationship between the measured magnetization and the relaxation parameters that is given by a 2D Fredholm equation. Moreover, higher dimensional (nD) relaxometry studies can also be used because compression efficiency can increase in CS with increased dimensionality particularly when spectral data are sparse and compactly supported, as appears to be the case with many experimental relaxation spectra. In addition, further data compression can be achieved if CS is used both in the Laplace domain, as is done here, and in the Fourier domain to reduce the number of MRI acquisitions required for spatial localization.

5. Conclusion

A new MR acquisition and analysis pipeline is proposed to vastly reduce the amount of 2D relaxation spectral data needed for material and tissue characterization applications without compromising data quality. This greater efficiency is achieved by reconstruction from incomplete 2D relaxation measurements with compressed sensing. This pipeline has been validated by 2D spectral simulations, NMR experiments on a well-characterized urea/water phantom, and T_1–T_2 relaxometry MRI experiments on a fixed porcine spinal cord. In addition to maintaining global correlations, the CS reconstruction from the incomplete measurements preserves other important parameters, including the local contrast between peaks and the amplitude and relaxation parameters of the peaks.

Acknowledgments

This work was supported by the Intramural Research Program (IRP) of the *Eunice Kennedy Shriver* National Institute of Child Health and Human Development, NIH. Alexander Cloninger is supported by the National Science Foundation under Award No. DMS-1402254. Thanks to Mrs. Joni Taylor, Mr. T.J. Hunt, and Mr. R.R. Clevenger from the ASR Core, NHLBI, for obtaining the spinal cord specimens and Ms. L. Salak for editing the manuscript. We are also

grateful to our colleagues Dr. Y. Gao for help preparing the urea/water phantom and Dr. M.E. Komlosh and Dr. E. Hutchinson for assistance with MRI experiment.

Appendix A. Recover $\widetilde{M}$ from incomplete measurements using compressed sensing

Let us start with the minimization problem in Eq. (3). With the SVD in Eq. (4), Eq. (3) can be rewritten as [28,39]

$$\begin{aligned}\widehat{F} &= \arg\min_{\widehat{F}\geqslant 0}\|M - K_1FK_2'\|^2 + \alpha\|F\|^2 \\ &= \arg\min_{\widehat{F}\geqslant 0}\left\|U_1\widehat{M}U_2' - U_1U_1'K_1FK_2'U_2U_2'\right\|^2 + \|M\|^2 \\ &\quad - \left\|U_1\widehat{M}U_2'\right\|^2 + \alpha\|F\|^2 \\ &= \arg\min_{\widehat{F}\geqslant 0}\left\|\widehat{M} - (S_1V_1')F(S_2V_2')'\right\|^2 + \alpha\|F\|^2 \end{aligned} \tag{A.1}$$

where the third line comes from U_1 and U_2 having orthogonal columns, and the second and the third items in the second line being independent of F. The target of the CS reconstruction is to search for a matrix X that well approximates the ground truth $\widetilde{M}_0 \equiv (S_1V_1')F(S_2V_2')' \in \mathbb{R}^{s_1\times s_2}$ with the given subsamples y, which was chosen from the full data M on random entries

$$y = \mathcal{R}_\Omega(\widetilde{M}_0) + \epsilon \tag{A.2}$$

where $\Omega \subset \{1,\ldots,N_1\}\times\{1,\ldots,N_2\}$ is the set of random indices where we observe M with $|\Omega| = m$ and the indices ordered as $\Omega = \{(i_k,j_k)\}_{k=1}^m$, and $\mathcal{R}_\Omega$ is the sampling operator

$$\begin{aligned}&\mathcal{R}_\Omega : \mathbb{R}^{s_1\times s_2} \to \mathbb{R}^m \\ &\mathcal{R}_\Omega(X) = \mathcal{A}_\Omega(U_1XU_2')\end{aligned} \tag{A.3}$$

Here $\mathcal{A}_\Omega$ is a linear operator with random sampling

$$\begin{aligned}&\mathcal{A}_\Omega : \mathbb{R}^{\boldsymbol{N}_1\times\boldsymbol{N}_2} \to \mathbb{R}^{\boldsymbol{m}} \\ &(\mathcal{A}_\Omega(X))_k = X_{i_k,j_k}\end{aligned} \tag{A.4}$$

Our CS reconstruction is based on low-rank matrix completion and the reconstruction step takes the form

$$\begin{aligned}&\min \quad \|X\|_* := \sum_{i=0}^{r}\sigma_i(X) \\ &\text{such that} \quad \|\mathcal{R}_\Omega(X) - y\|_2 \leqslant \epsilon\end{aligned} \tag{A.5}$$

where $\sigma_i(X)$ is the ith singular value of a rank r matrix X and the operator $\mathcal{R}_\Omega$ satisfies the restricted isometry property (RIP) as demonstrated in [39]. In the algorithm, instead of solving Eq. (A.5), we solved the relaxed Lagrangian form

$$\min \mu\|X\|_* + \frac{1}{2}\|\mathcal{R}_\Omega(X) - y\|_2^2 \tag{A.6}$$

Eq. (A.6) is solved using the singular value thresholding algorithm from [45,49] with a two-step iterative process. Let the matrix derivative of the L_2 norm term in Eq. (A.6) be written as

$$g(X) = \mathcal{R}_\Omega^*(\mathcal{R}_\Omega(X) - y) = U_1'(\mathcal{A}_\Omega^*(\mathcal{A}_\Omega(U_1XU_2') - y))U_2 \tag{A.7}$$

Another notation is the singular value thresholding operator S_v that reduces each singular value of some matrix X by v. Let us say the SVD of X is $X = U\Sigma V'$, then S_v is defined as

$$S_v(X) = U\hat{\Sigma}V', \text{ with } \hat{\Sigma}_{i,j} = \begin{cases}\max(\Sigma_{i,i} - v, 0), & i = j \\ 0, & \text{otherwise}\end{cases} \tag{A.8}$$

The two-step iterative process is then

$$\begin{cases} Y^k = X^k - \tau g(X^k) \\ X^{k+1} = S_{\tau v}(Y^k)\end{cases} \tag{A.9}$$

With proper choices of τ and μ, for any initial condition, this method converges with a high probability to a matrix $\widehat{M}$, which is guaranteed in theorem [39] to be close to $\widetilde{M}$ up to a constant factor of the noise. The recovered $\widehat{M}$ is then substituted into Eq. (A.1) to solve for F. More details about this CS reconstruction process can be found in [39].

References

[1] G.S. Rule, T.K. Hitchens, Fundamentals of Protein NMR Spectroscopy, Springer, Dordrecht, 2006.
[2] M.D. Does, J.C. Gore, Compartmental study of T 1 and T 2 in rat brain and trigeminal nerve in vivo, Magn. Reson. Med. 47 (2002) 274–283.
[3] P. Galvosas, Y. Qiao, M. Schönhoff, P.T. Callaghan, On the use of 2D correlation and exchange NMR spectroscopy in organic porous materials, Magn. Reson. Imaging 25 (2007) 497–500.
[4] R.D. Dortch, G.A. Apker, W.M. Valentine, B. Lai, M.D. Does, Compartment-specific enhancement of white matter and nerve ex vivo using chromium, Magn. Reson. Med. 64 (2010) 688–697.
[5] A.E. English, K.P. Whittall, M.L.G. Joy, R.M. Henkelman, Quantitative two-dimensional time correlation relaxometry, Magn. Reson. Med. 22 (1991) 425–434.
[6] G. Saab, R.T. Thompson, G.D. Marsh, P.A. Picot, G.R. Moran, Two-dimensional time correlation relaxometry of skeletal muscle in vivo at 3 Tesla, Magn. Reson. Med. 46 (2001) 1093–1098.
[7] D. van Dusschoten, C.T.W. Moonen, P.A. de Jager, H. Van As, Unraveling diffusion constants in biological tissue by combining Carr–Purcell–Meiboom–Gill imaging and pulsed field gradient NMR, Magn. Reson. Med. 36 (1996) 907–913.
[8] J.G. Seland, M. Bruvold, H. Anthonsen, H. Brurok, W. Nordhøy, P. Jynge, J. Krane, Determination of water compartments in rat myocardium using combined D-T1 and T1–T2 experiments, Magn. Reson. Imaging 23 (2005) 353–354.
[9] J. Warner, S. Donell, K. Wright, L. Venturi, B. Hills, The characterisation of mammalian tissue with 2D relaxation methods, Magn. Reson. Imaging 28 (2010) 971–981.
[10] L. Venturi, J. Warner, B. Hills, Multisliced ultrafast 2D relaxometry, Magn. Reson. Imaging 28 (2010) 964–970.
[11] P.S. Belton, A.M. Gil, G.A. Webb, D. Rutledge, Magnetic Resonance in Food Science. Latest Developments, Royal Society of Chemistry, Bedford, UK, 2003.
[12] M.D. Hürlimann, L. Burcaw, Y.-Q. Song, Quantitative characterization of food products by two-dimensional D-T2 and T1–T2 distribution functions in a static gradient, J. Colloid Interface Sci. 297 (2006) 303–311.
[13] P.T. Callaghan, I. Furó, Diffusion-diffusion correlation and exchange as a signature for local order and dynamics, J. Chem. Phys. 120 (2004) 4032–4038.
[14] A.M. Olaru, J. Kowalski, V. Sethi, B. Blümich, Exchange relaxometry of flow at small Péclet numbers in a glass bead pack, J. Magn. Reson. 220 (2012) 32–44.
[15] Y. Qiao, P. Galvosas, T. Adalsteinsson, M. Schönhoff, P.T. Callaghan, Diffusion exchange NMR spectroscopic study of dextran exchange through polyelectrolyte multilayer capsules, J. Chem. Phys. 122 (2005) 214912.
[16] L. Venturi, N. Woodward, D. Hibberd, N. Marigheto, A. Gravelle, G. Ferrante, B.P. Hills, Multidimensional cross-correlation relaxometry of aqueous protein systems, Appl. Magn. Reson. 33 (2008) 213–234.
[17] L. Monteilhet, J.-P. Korb, J. Mitchell, P. McDonald, Observation of exchange of micropore water in cement pastes by two-dimensional T2–T2 nuclear magnetic resonance relaxometry, Phys. Rev. E 74 (2006) 061404.
[18] K. Washburn, P. Callaghan, Tracking pore to pore exchange using relaxation exchange spectroscopy, Phys. Rev. Lett. 97 (2006) 175502.
[19] M. Gratz, M. Wehring, P. Galvosas, F. Stallmach, Multidimensional NMR diffusion studies in microporous materials, Microporous Mesoporous Mater 125 (2009) 30–34.
[20] A.R. Mutina, M.D. Hürlimann, Correlation of transverse and rotational diffusion coefficient: a probe of chemical composition in hydrocarbon oils, J. Phys. Chem. A 112 (2008) 3291–3301.
[21] M.D. Hürlimann, M. Flaum, L. Venkataramanan, C. Flaum, R. Freedman, G.J. Hirasaki, Diffusion–relaxation distribution functions of sedimentary rocks in different saturation states, Magn. Reson. Imaging 21 (2003) 305–310.
[22] P.T. Callaghan, C.H. Arns, P. Galvosas, M.W. Hunter, Y. Qiao, K.E. Washburn, Recent Fourier and Laplace perspectives for multidimensional NMR in porous media, Magn. Reson. Imaging 25 (2007) 441–444.
[23] R.D. Dortch, R.A. Horch, M.D. Does, Development, simulation, and validation of NMR relaxation-based exchange measurements, J. Chem. Phys. 131 (2009) 164502.
[24] L. Venturi, K. Wright, B. Hills, Ultrafast T1–T2 relaxometry using FLOP sequences, J. Magn. Reson. 205 (2010) 224–234.
[25] B. Sun, K.-J. Dunn, A global inversion method for multi-dimensional NMR logging, J. Magn. Reson. 172 (2005) 152–160.
[26] D. Bernin, D. Topgaard, NMR diffusion and relaxation correlation methods: new insights in heterogeneous materials, Curr. Opin. Colloid Interface Sci. 18 (2013) 166–172.

[27] Y.-Q. Song, L. Venkataramanan, M.D. Hürlimann, M. Flaum, P. Frulla, C. Straley, T(1)–T(2) correlation spectra obtained using a fast two-dimensional Laplace inversion, J. Magn. Reson. 154 (2002) 261–268.
[28] L. Venkataramanan, Y. Song, M.D. Hürlimann, Solving Fredholm integrals of the first kind with tensor product structure in 2 and 2. 5 dimensions, J. Magn. Reson. 50 (2002) 1017–1026.
[29] N. Marigheto, L. Venturi, D. Hibberd, K.M. Wright, G. Ferrante, B.P. Hills, Methods for peak assignment in low-resolution multidimensional NMR cross-correlation relaxometry, J. Magn. Reson. 187 (2007) 327–342.
[30] E.W. Abel, T.P.J. Coston, K.G. Orrell, V. Sik, D. Stephenson, Two-dimensional NMR exchange spectroscopy. quantitative treatment of multisite exchanging systems, J. Magn. Reson. 70 (1986) 34–53.
[31] J. Mitchell, T.C. Chandrasekera, L.F. Gladden, Numerical estimation of relaxation and diffusion distributions in two dimensions, Prog. Nucl. Magn. Reson. Spectrosc. 62 (2012) 34–50.
[32] E.J. Candes, M.B. Wakin, An introduction to compressive sampling, IEEE Signal Process. Mag. 25 (2008) 21–30.
[33] M. Doneva, P. Börnert, H. Eggers, C. Stehning, J. Sénégas, A. Mertins, Compressed sensing reconstruction for magnetic resonance parameter mapping, Magn. Reson. Med. 64 (2010) 1114–1120.
[34] C. Huang, C.G. Graff, E.W. Clarkson, A. Bilgin, M.I. Altbach, T2 mapping from highly undersampled data by reconstruction of principal component coefficient maps using compressed sensing, Magn. Reson. Med. 67 (2012) 1355–1366.
[35] M. Lustig, D. Donoho, J.M. Pauly, Sparse MRI: the application of compressed sensing for rapid MR imaging, Magn. Reson. Med. 58 (2007) 1182–1195.
[36] M.I. Menzel, E.T. Tan, K. Khare, J.I. Sperl, K.F. King, X. Tao, C.J. Hardy, L. Marinelli, Accelerated diffusion spectrum imaging in the human brain using compressed sensing, Magn. Reson. Med. 66 (2011) 1226–1233.
[37] C. Prieto, M.E. Andia, C. von Bary, D.C. Onthank, T. Schaeffter, R.M. Botnar, Accelerating three-dimensional molecular cardiovascular MR imaging using compressed sensing, J. Magn. Reson. Imaging 36 (2012) 1363–1371.
[38] E. Candès, J. Romberg, Sparsity and incoherence in compressive sampling, Inverse Probl. 23 (2007) 969–985.
[39] A. Cloninger, W. Czaja, R. Bai, P.J. Basser, Solving 2D Fredholm integral from Incomplete measurements using compressive sensing, SIAM J. Imaging Sci. 7 (2014) 1775–1798.
[40] R.A. Horch, M.D. Does, Aqueous urea as a model system for bi-exponential relaxation, Magn. Reson. Mater. Phys., Biol. Med. 20 (2007) 51–56.
[41] R. Bai, C.G. Koay, E. Hutchinson, P.J. Basser, A framework for accurate determination of the T2 distribution from multiple echo magnitude MRI images, J. Magn. Reson. 244 (2014) 53–63.
[42] C.G. Koay, E. Özarslan, C. Pierpaoli, Probabilistic identification and estimation of noise (PIESNO): a self-consistent approach and its applications in MRI, J. Magn. Reson. 199 (2009) 94–103.
[43] C.G. Koay, E. Özarslan, P.J. Basser, A signal transformational framework for breaking the noise floor and its applications in MRI, J. Magn. Reson. 197 (2009) 108–119.
[44] J.P. Butler, J.A. Reeds, S.V. Dawson, Estimating solutions of first kind integral equations with nonnegative constraints and optimal smoothing, SIAM J. Numer. Anal. 18 (1981) 381–397.
[45] J.-F. Cai, E.J. Candès, Z. Shen, A singular value thresholding algorithm for matrix completion, SIAM J. Optim. 20 (2010) 1956–1982.
[46] A.R. Travis, M.D. Does, Selective excitation of myelin water using inversion-recovery-based preparations, Magn. Reson. Med. 54 (2005) 743–747.
[47] A. MacKay, C. Laule, I. Vavasour, T. Bjarnason, S. Kolind, B. Mädler, Insights into brain microstructure from the T2 distribution, Magn. Reson. Imaging 24 (2006) 515–525.
[48] R. Harrison, M.J. Bronskill, R. Mark Henkelman, R.M. Henkelman, Magnetization transfer and T2 relaxation components in tissue, Magn. Reson. Med. 33 (1995) 490–496.
[49] S. Ma, D. Goldfarb, L. Chen, Fixed point and Bregman iterative methods for matrix rank minimization, Math. Program. 128 (2009) 321–353.